nature chemistry

Article

https://doi.org/10.1038/s41557-024-01464-6

Silicon-RosIndolizine fluorophores with shortwave infrared absorption and emission profiles enable in vivo fluorescence imaging

Received: 6 December 2022

Accepted: 29 January 2024

Published online: 25 March 2024

Check for updates

William E. Meador[1,5], Eric Y. Lin[2,5], Irene Lim[2], Hannah C. Friedman[2], David Ndaleh[1], Abdul K. Shaik[1], Nathan I. Hammer[1], Boqian Yang[3], Justin R. Caram[2], Ellen M. Sletten[2] ✉ & Jared H. Delcamp[1,4] ✉

In vivo fluorescence imaging in the shortwave infrared (SWIR, 1,000–1,700 nm) and extended SWIR (ESWIR, 1,700–2,700 nm) regions has tremendous potential for diagnostic imaging. Although image contrast has been shown to improve as longer wavelengths are accessed, the design and synthesis of organic fluorophores that emit in these regions is challenging. Here we synthesize a series of silicon-RosIndolizine (SiRos) fluorophores that exhibit peak emission wavelengths from 1,300–1,700 nm and emission onsets of 1,800–2,200 nm. We characterize the fluorophores photophysically (both steady-state and time-resolved), electrochemically and computationally using time-dependent density functional theory. Using two of the fluorophores (SiRos1300 and SiRos1550), we formulate nanoemulsions and use them for general systemic circulatory SWIR fluorescence imaging of the cardiovascular system in mice. These studies resulted in high-resolution SWIR images with well-defined vasculature visible throughout the entire circulatory system. This SiRos scaffold establishes design principles for generating long-wavelength emitting SWIR and ESWIR fluorophores.

Biomedical imaging is an invaluable tool in the hands of research scientists and medical professionals. It allows for the visualization of internal structures, diagnosis of diseases and injuries, and provides spatial information on bodily regions of interest. Of the types of imaging modalities currently available, shortwave infrared (SWIR, 1,000–1,700 nm; sometimes referred to as the second and third near-infrared regions; NIR-II and NIR-III, respectively)[1–3] fluorescence imaging offers several advantages over traditional forms of in vivo imaging in that it avoids harmful ionizing radiation, can provide high spatiotemporal resolution, enables targeted imaging of specific diseases/regions and provides rapid data acquisition[4–9]. Magnetic and high-energy radiation techniques underperform at one or more of these desirable capabilities[4,5,10]. In this way, SWIR fluorescence imaging has the capacity to be a specific, rapid, non-toxic and high-resolution technique for in vivo imaging with promising biomedical applications. Improvements to organic dye properties are needed to realize this type of imaging, especially with regard to accessing longer wavelengths.

Compared with visible light, light in the SWIR and extended SWIR (ESWIR 1,700–2,700 nm, including the rarely accessed NIR-IV region, in which the total attenuation coefficients of tissues are smallest)[11–13] regions offers several advantages for full body in vivo imaging by limiting light scattering, absorption and the autofluorescence of

[1]University of Mississippi, Department of Chemistry and Biochemistry, Oxford, MS, USA. [2]University of California Los Angeles, Department of Chemistry and Biochemistry, Los Angeles, CA, USA. [3]HORIBA Scientific, Piscataway, NJ, USA. [4]Air Force Research Laboratory, Materials and Manufacturing Directorate (RXNC), Wright-Patterson AFB, Dayton, OH, USA. [5]These authors contributed equally: William E. Meador, Eric Y. Lin. ✉e-mail: Sletten@chem.ucla.edu; delcamp@olemiss.edu

https://doi.org/10.1038/s41557-024-01464-6

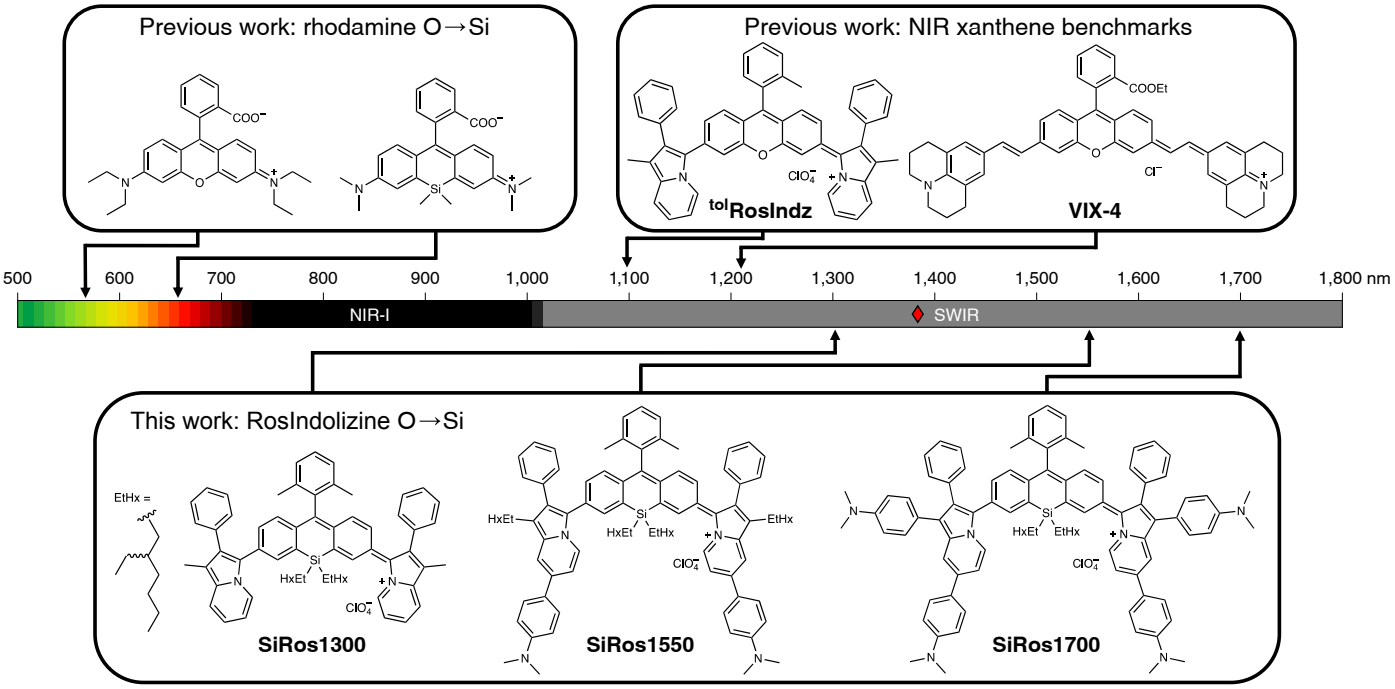

Fig. 1 | Emission maxima of xanthene and silicon-substituted xanthene-based fluorophores. Structure of xanthene and silicon-substituted xanthene-based fluorophores with alkyl amine donors from the literature (top-left box), xanthene-based fluorophores with heterocyclic donors from the literature (top-right box) and SiRos fluorophores presented herein (bottom box). Respective emission maxima are indicated by arrows. The small-molecule fluorophore with longest wavelength emission maxima reported so far is shown as a red diamond on the scale as a benchmark[29].

biological tissues[4]. These factors impede excitation light penetration and the contrast of the image obtained[14]. Although PbS quantum dots and cerium-based materials have been shown to exhibit peak emission past 1,400 nm, these materials are toxic, making them undesirable for in vivo applications[15,16]. To the best of our knowledge, there are no organic small-molecule fluorophores with peak emission beyond 1,400 nm, despite the great potential for increased image quality. Weak tail emissions are currently used to generate images beyond 1,400 nm from organic small molecules[17–19].

Organic fluorophores are extremely diverse with a range of classes offering tunable spectral properties. Although there is an abundance of organic fluorophores that absorb and emit in the NIR (700–1,000 nm), there are still only a handful that absorb and emit in the SWIR. These SWIR organic fluorophores have provided the highest resolution in vivo fluorescence images so far. Until recently, xanthene-type fluorophores such as fluorescein and rhodamine were generally considered visible-region fluorophores[20]. A SWIR-peak-emitting xanthene-based fluorophore was recently synthesized by installing indolizine heterocycles in place of alkyl amine donors, resulting in a ~400 nm (1.01 eV) bathochromic shift in the absorbance of the material to 930 nm and a SWIR emission maximum at 1,092 nm (ref. 21). Soon thereafter, *para*-functionalized styrene-based donors were used to yield a set of fluorophores with remarkably low-energy emission maxima at 1,210 nm (ref. 9). These molecules were observed to yield rapid, high-resolution in vivo SWIR fluorescence images of vascular tissues via encapsulation of the fluorophores in a micelle. This approach has led to several reports on SWIR-emitting xanthene-type fluorophores, including the discovery of a 1,256-nm-emitting fluorophore made possible by indolizine-donor-group tuning via the addition of *N,N*-dimethylaniline (DMA) groups to the heterocycle periphery[22,23]. Modification of the xanthene core by replacing oxygen with silicon is known to induce bathochromic shifts in peak emission by ~90 nm (0.34 eV; Fig. 1)[24–28]. Here we investigate the combination of a silicon-substituted xanthene core with DMA-decorated indolizine donors to access longer wavelengths for absorption and emission. Through this approach we generate long-wavelength emitting small-molecule organic fluorophores that extend >300 nm beyond the current state of the art, with emission onsets (defined as 5% maximum emission intensity value) extending into the ESWIR region (Fig. 1)[9,29,30].

Results and discussion

Fluorophore design and synthesis

Synthesis of the silicon-RosIndolizine (SiRos) dyes makes use of each of the three distinct halides of 2-bromo-4-chloro-1-iodobenzene iteratively to build the SiRos core and install donor functionality (Fig. 2). Alcohol **1** is synthesized as previously reported from 2-bromo-4-chloro-1-iodobenzene and 2-bromo-4-chlorobenzaldehyde[31]; **1** is subsequently deoxygenated with BF_3/$SiEt_3H$ to give diarylmethane **2** in 99% yield. Double lithium-bromide exchange with **2** is used to form a cyclized silane intermediate when reacted with dichlorobis(2-ethylhexyl)silane. This crude intermediate is oxidized with $KMnO_4$ to give the ketone product **3** in 37% overall yield. The 2-ethylhexyl substituent was chosen to (1) incorporate solubilizing groups to the core to aid in synthetic ease, (2) increase sterics of the fluorophore to diminish aggregation and (3) incorporate bulky groups to slow nucleophilic attack at the core as was observed in previous iterations of indolizine-xanthene fluorophores[32]. C–H activation of the indolizine donor groups, **4**–**6** (synthesized as previously reported)[33,34], is performed using aryl chloride **3** and a palladium catalyst to yield the silicon-substituted xanthones, **7**–**9**, in 46–88% yield. The final dyes are synthesized via a one-pot reaction sequence beginning with a Grignard reaction using 2,6-dimethylphenylmagnesium bromide to yield the alcohol intermediates, followed by formation of the fluorophore via acidic work-up with 2 M $HClO_4$ (aq). Installation of the xylyl group via the Grignard reaction is an integral component of dye design, as larger *ortho* groups about the xanthene core have demonstrated increased

https://doi.org/10.1038/s41557-024-01464-6

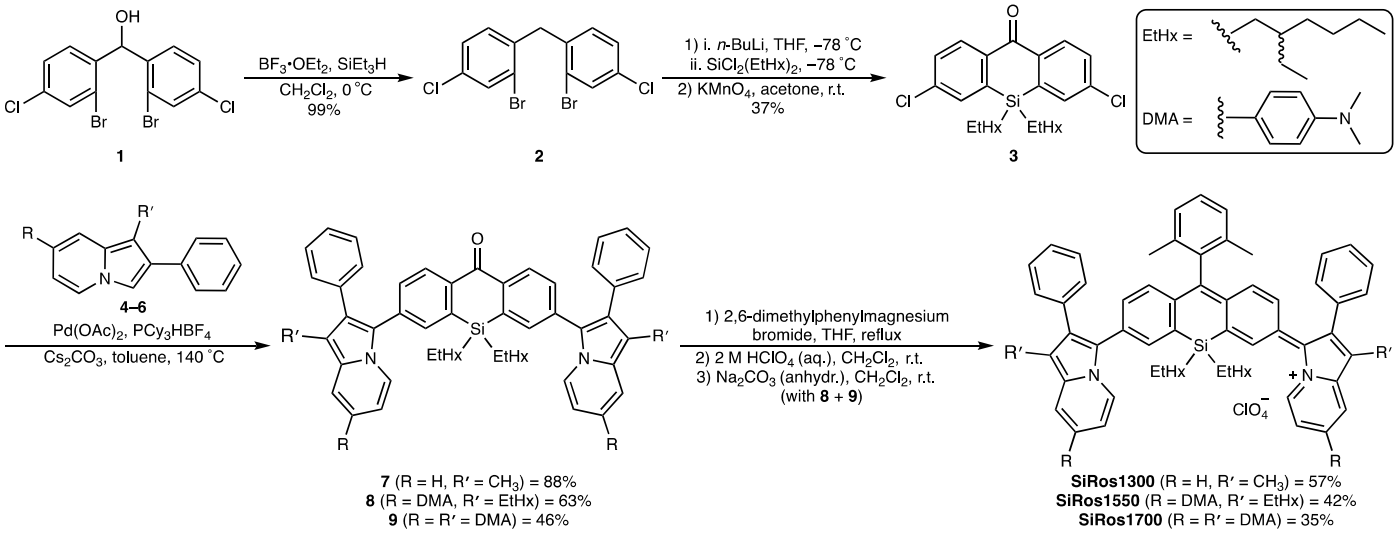

Fig. 2 | Full synthetic route to SiRos1300, SiRos1550 and SiRos1700. Synthesis of the SiRos fluorophores begins with a deoxygenation reaction followed by a silylation cyclization reaction and subsequent oxidation to yield the silicon-substituted xanthene core. A palladium-catalysed C–H activation reaction is then used to install the respective indolizine donors. A Grignard reaction followed by an acidic work-up yields the final SiRos fluorophores as the perchlorate salt. Further work-up over anhydrous base is required for the SiRos dyes containing DMA groups. EtHx is 2-ethylhexyl abbreviated.

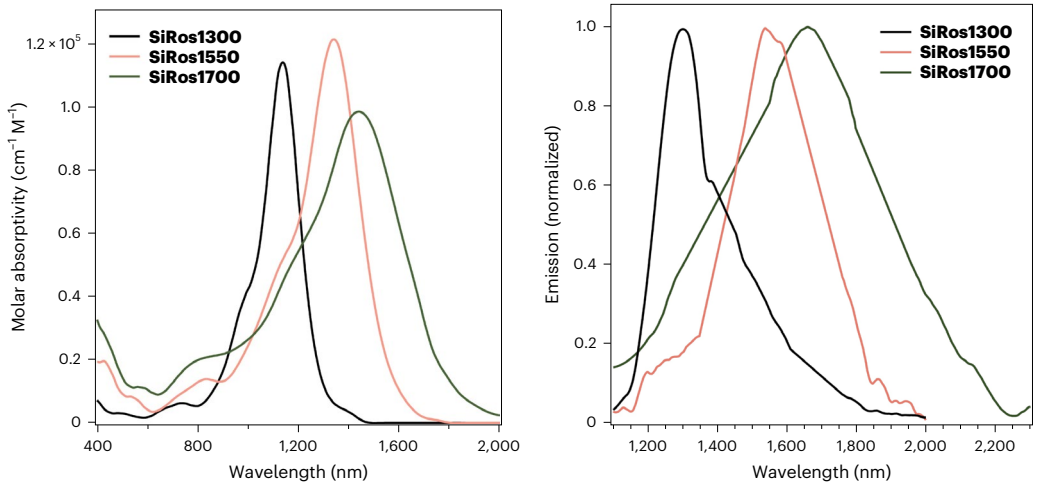

Fig. 3 | Molar absorptivity and normalized emission of SiRos1300, SiRos1550 and SiRos1700. Molar absorptivity spectra (left) and normalized and solvent-reabsorption-corrected emission spectra (right) of the fluorophores in a 1×10^{-5} M solution of CH_2Cl_2.

stability towards hydrolytic decomposition[22,23,32]. Although **SiRos1300** is isolable directly from the acid work-up, **SiRos1550** and **SiRos1700** require an additional biphasic reaction in dichloromethane (CH_2Cl_2) over anhydrous Na_2CO_3 to deprotonate the DMA groups. This process is monitored via absorption spectroscopy as the protonated amine derivates demonstrate a nearly identical absorption to **SiRos1300**, and a bathochromic shift in the absorption spectrum is observed as the deprotonation reaction proceeds. With **SiRos1300**, **SiRos1550** and **SiRos1700** in hand, their photophysical properties were studied.

Steady-state absorption and emission spectroscopy

Absorption spectroscopy reveals remarkably low-energy maxima at 1,140 nm, 1,348 nm and 1,440 nm for **SiRos1300, SiRos1550** and **SiRos1700** in CH_2Cl_2, respectively (Fig. 3). The exchange in the xanthene core from oxygen to silicon results in a bathochromic shift in the absorbance maxima of 0.25 eV (210 nm) from the previously reported ^{tol}RosIndz to **SiRos1300**, which is comparable with past literature reports of a bathochromic shift of 0.34 eV (90 nm) observed for traditional rhodamine dyes with alkyl amine donors (Fig. 1)[35]. **SiRos1550** has the largest molar absorptivity (ε) in CH_2Cl_2 of the dye series, at 122,000 $M^{-1}\,cm^{-1}$, with **SiRos1300** and **SiRos1700** at 115,000 $M^{-1}\,cm^{-1}$ and 98,000 $M^{-1}\,cm^{-1}$, respectively (Table 1). As observed previously for the 1,7-DMA indolizine donor[34], the steric interaction between the additional DMA at the 1-position of indolizine and the phenyl ring at the 2-position lowers the molar absorptivity of **SiRos1700** to 98,000 $M^{-1}\,cm^{-1}$, resulting in a broadened absorption profile compared with **SiRos1300** and **SiRos1550**. Although all dyes are nearly black when concentrated, **SiRos1300** is colourless, **SiRos1550** is orange and **SiRos1700** is green at concentrations used for absorption and emission spectroscopy (~1×10^{-5} M) due to higher-energy visible-region absorption bands. The absorption of the dyes in acetonitrile (CH_3CN) is also studied to understand how increasing solvent polarity affects the photophysical properties of the dyes (Table 1 and Supplementary Fig. 2). For all dyes, the absorption profiles are observed to broaden and shift towards higher energy in CH_3CN, and ε decreases to just over half of what is observed in CH_2Cl_2. Overall, the

Table 1 | Photophysical data of SiRos1300, SiRos1550 and SiRos1700 in the specified solvents

Dye	Solvent	λ_{abs}^{max} (nm)	λ_{emis}^{max} (nm)	λ_{emis}^{onset} (nm)	ε ($M^{-1}cm^{-1}$)	Φ_F (%)	Molecular brightness ($M^{-1}cm^{-1}$)
SiRos1300	CH_2Cl_2	1,140	1,300	1,800	115,000	0.0056±0.0007	6.4
	CH_3CN	1,116	—		45,000	—	—
	D_2O*	1,117	1,241	1,800	35,000	0.0068±0.0009	2.4
SiRos1550	CH_2Cl_2	1,348	1,557	2,000	122,000	0.0025±0.0003	3.1
	CH_3CN	1,293	—		61,000	—	—
	D_2O*	1,211	1,475	>1,900	51,000	0.0021±0.0003	1.1
SiRos1700	CH_2Cl_2	1,440	~1,700	2,200	98,000	0.0011±0.0003	1.1
	CH_3CN	1,280	—		54,000	—	—
	D_2O*	1,053	1,500	2,200	59,000	0.0007±0.0001	0.4
ICG[57]	Ethanol	787	818	~1,000	194,000	13.2±0.8	25,600
FD-1029[58]	Ethanol	981	1,022	—	186,000	0.58	1,055
VIX-4[9]	CH_2Cl_2	1,014	1,210	~1,700	219,000	0.008±0.0009	18
Flav7[38,54]	CH_2Cl_2	1,027	1,053	~1,300	241,000	0.61±0.02	1,470
IR-1061[38,59]	CH_2Cl_2	1,063	1,081	~1,400	325,000	0.32±0.04	1,040
IR-26[37]	$C_2H_4Cl_2$	1,084	1,144	~1,450	130,000	0.05±0.003	65
7-DMA-RI[23]	Toluene	1,096	1,256	~1,600	71,000	0.005	4
NIR1380[29]	CH_2Cl_2	1,270	1,380	1,700	—	0.14	—
HC1376[30]	$C_2H_4Cl_2$	1,312	1,376	~1,700	91,880	0.011	10.1

*Inside of a DSPE-mPEG2000 micelle. Determination of the quantum yield error is discussed in the Methods.

lower molar absorptivity, shift towards higher energy and broadening of the absorption features indicate that the dyes may begin to transition from a $\pi \rightarrow \pi^*$ system to a $n \rightarrow \pi^*$ charge transfer system as the solvent polarity increases. The absorptions of the dyes are also studied while inside of a DSPE-mPEG2000 micelle in D_2O solution (due to the longer-wavelength absorption of D_2O relative to H_2O)[36] to observe how the dyes absorb light inside of a mimicked aqueous micellar environment (Supplementary Fig. 3). Similar to the absorption spectra of the dyes in CH_3CN, the absorption spectra of the dyes in the micelle are observed to broaden and decrease in intensity compared with CH_2Cl_2. The broadened absorption in a micellular-D_2O environment may be due to aggregate formation or increased solvent polarity.

The emission spectra and fluorescent quantum yields (Φ_F) of **SiRos1300**, **SiRos1550** and **SiRos1700** were measured in CH_2Cl_2 (Fig. 3, Table 1 and Supplementary Figs. 5–7). The dyes have peak emission values (λ_{emis}^{max}) of 1,300 nm, 1,557 nm and ~1,700 nm for **SiRos1300**, **SiRos1550** and **SiRos1700**, respectively. All of the dyes have emission onsets (λ_{emis}^{onset}) within the ESWIR region: 1,800 nm, 2,000 nm and 2,200 nm for **SiRos1300**, **SiRos1550** and **SiRos1700**, respectively. Currently, the lowest-energy λ_{emis}^{max} value for an organic small molecule is observed at 1,380 nm to the best of our knowledge (ref. 29), which **SiRos1550** and **SiRos1700** both surpass by ~170 nm and ~320 nm, respectively. The emission spectra of the materials in CH_2Cl_2 generally mirror the absorption spectra, demonstrating that the shoulder features seen in the absorption spectra are vibronic in nature. The emission spectra in CH_2Cl_2 also demonstrate sharp decreases in emission intensity in several places, the most prominent of which occurs at 1,700 nm (Fig. 3 and Supplementary Figs. 5–7). These sharp decreases in emission intensity align with the absorption spectrum of CH_2Cl_2 and are attributed to solvent reabsorption, as has been seen previously for SWIR-emitting materials (Supplementary Figs. 5–7)[37]. Herein, solvent reabsorption corrections were performed as outlined in the Methods to bring clarity to the emission spectra (Supplementary Fig. 8–10). The Φ_F of **SiRos1300** was found to be 0.0056 ± 0.0007% in CH_2Cl_2 (referenced with respect to an IR-1061 Φ_F of 0.32 ± 0.04% in CH_2Cl_2) using equations (4) and (5) in the Methods[38]. The Φ_F of IR-1061 was selected as the standard due to its thorough characterization in the literature, where several methods were used to show the wide variation of Φ_F reference values obtainable for this dye[38]. One of the most common reference dyes (IR-26) in the SWIR has Φ_F reference values that range by an order of magnitude in the literature; thus, comparing Φ_F values between papers requires care[17,39]. All other dyes in the series were then referenced with respect to **SiRos1300** in CH_2Cl_2 (Table 1). **SiRos1550** was measured to have a Φ_F of 0.0025 ± 0.0003% (roughly half that of **SiRos1300**), whereas **SiRos1700** was measured to have a Φ_F of 0.0011 ± 0.0003% (roughly half that of **SiRos1550**). The Φ_F values found herein are for the raw emission spectra and would increase slightly after solvent-reabsorption corrections because both **SiRos1550** and **SiRos1700** have considerable portions of their integrated emission intensity missing due to solvent reabsorption (Supplementary Figs. 5–7). Emission spectra were also collected inside of a DSPE-mPEG2000 micelle in D_2O to understand the molecular brightness of the dyes in an aqueous micellular environment (Supplementary Fig. 4). D_2O was selected as a solvent because it absorbs light at ~300 nm longer wavelengths than H_2O (refs. 36,40). The values of Φ_F inside of the micelle were observed to be 0.0068 ± 0.0009%, 0.0021 ± 0.0003% and 0.0007 ± 0.0001% for **SiRos1300**, **SiRos1550** and **SiRos1700**, respectively. It should be stressed that there are no organic small-molecule

Table 2 | Photoluminescent lifetimes, Stokes shifts, absorption and emission oscillator strengths, transition dipole moments, and degeneracy ratios of SiRos fluorophores

	Lifetime (ps)	E_{Stokes} (cm^{-1})	f_{12}	f_{21}	μ_{21} (D)	g_2/g_1
SiRos1300	20	1,080	1.14	−0.028	3.3	41
SiRos1550	26	996	1.15	−0.014	2.5	84
SiRos1700	47	1,052	1.07	−0.004	1.4	270

https://doi.org/10.1038/s41557-024-01464-6

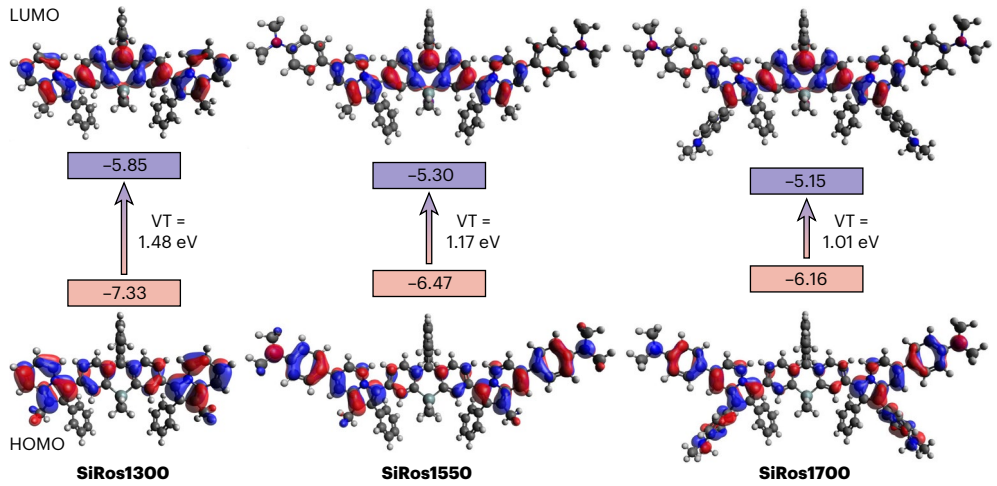

Fig. 4 | Frontier molecular orbital analysis of the SiRos fluorophores. HOMO (bottom) and LUMO (top) orbital density plots of **SiRos1300**, **SiRos1550** and **SiRos1700**, computed at the B3LYP/6-311 G(*d*,*p*) level of theory using CH_2Cl_2 as an implicit solvent. Computed energies of the HOMO and LUMO orbitals and the vertical transitions (VT) are provided along with each fluorophore.

materials that emit in this spectral region (>1,400 nm) to the best of our knowledge and that the signal-to-noise ratio in the SWIR is heavily wavelength dependent, making lower-energy emission more valuable than the sacrifice of signal intensity[41].

We observed λ_{emis}^{max} of 1,241 nm, 1,475 nm and 1,500 nm for **SiRos1300**, **SiRos1550** and **SiRos1700** in D_2O, respectively (Table 1 and Supplementary Fig. 4). Once again, the emission spectra of both **SiRos1550** and **SiRos1700** surpass the previous lowest energy observed λ_{emis}^{max} (in CH_2Cl_2) by ~95 and ~120 nm, respectively. The emission spectra of **SiRos1300**, **SiRos1550** and **SiRos1700** in D_2O do not mirror the absorption spectra, which is probably due to the non-emissive aggregate states of the dyes being present in the micelle that are responsible for light absorption but not fluorescence emission. The emission spectrum of **SiRos1550** and **SiRos1700** seem to cut off sharply in D_2O at ~1,900 nm due to the strong absorption feature of D_2O at 1,900 nm (Supplementary Figs. 11–13). The λ_{emis}^{onset} values in D_2O are similar to those observed in CH_2Cl_2 for **SiRos1300** and **SiRos1700** at 1,800 nm and 2,200 nm, respectively; however, the λ_{emis}^{onset} of **SiRos1550** is not observable due to the absorption of the D_2O solvent and is estimated herein to be >1,900 nm. Although the λ_{emis}^{onset} of **SiRos1700** is similarly impacted by the absorption of D_2O, it demonstrates observable emission intensity past the D_2O absorption feature, revealing the true emission onset to be 2200 nm. Overall, all three dyes demonstrate appreciable emission in the SWIR in both organic solvent and aqueous micelles and show promise as SWIR organic small molecule imaging materials.

Molecular brightness (MB = $\varepsilon \times \Phi_F$) is defined as the product of the molar absorptivity and the fluorescence quantum yield of a material; it is a useful metric for comparing the relative brightness of fluorophores as it accounts for both how much light a fluorophore absorbs and how efficiently it subsequently emits that light. Molecular brightness values of 6.4 $M^{-1}\,cm^{-1}$, 3.1 $M^{-1}\,cm^{-1}$ and 1.1 $M^{-1}\,cm^{-1}$ were observed for **SiRos1300**, **SiRos1550** and **SiRos1700**, respectively, in CH_2Cl_2 (Table 1). These values are a similar to those observed for other SWIR-emitting xanthene fluorophores[9] such as VIX-4 when the large bathochromic shifts of the SiRos materials are considered.

Photoluminescent lifetimes

Photoluminescent lifetimes of the SiRos dyes were determined to further understand the photophysical characteristics and excited-state kinetics of the materials (Table 2 and Supplementary Fig. 17). Upon excitation with a 785 nm laser, emitted photons were detected and timed using superconducting nanowire single-photon detectors (which are sensitive to light from 800–2,500 nm) with >30% quantum efficiency and sub 100 ps instrument response[42]. Interestingly, the lifetimes were observed to be inversely proportional to the emission energy of the fluorophores, with **SiRos1300** having the shortest deconvolved lifetime of 20 ps, and **SiRos1700** having the longest lifetime of 47 ps. These results are counter-intuitive to previous observations of bathochromic shifts in fluorophores coinciding with increased non-radiative decay rates due to the energy gap law[41,43–46]. There is no trend in Stokes shift (E_{Stokes}), indicating similar coupling to vibrational modes between chromophores. Furthermore, solvent reabsorption is known to decrease lifetimes due to direct energy transfer from chromophore to solvent vibrational modes[47]. Thus, the lengthening of lifetimes at longer wavelengths is even more surprising given these mitigating factors.

Combining Φ_F, lifetime and absorption spectrum information, we observed that the radiative rate decreases from **SiRos1300** to **SiRos1700** ($2.8 \times 10^6\ s^{-1}$ and $2.34 \times 10^5\ s^{-1}$, respectively), whereas non-radiative rates only slightly decrease ($5 \times 10^{10}\ s^{-1}$ and $2.13 \times 10^{10}\ s^{-1}$, respectively). The change in Φ_F is therefore almost entirely attributable to changes in the radiative rates (k_r). Indeed, the measured transition dipole moment (μ_{21}) and the absolute value of oscillator strength of emission (f_{21}) decreases as the chromophores undergo a bathochromic shift, with μ_{21} values decreasing from 3.3 to 1.4 D, and f_{21} values decreasing from −0.028 to −0.004, through applications of radiative rate law (equations (1) and (2)) below:

$$\mu_{21} = \sqrt{\frac{3\hbar^4 c^3}{4E_g^3 \eta} k_r} \tag{1}$$

and

$$f_{21} = -\frac{2\pi\epsilon_0 m\hbar^2 c^3}{qE_g^2 \eta} k_r \tag{2}$$

Where E_g is the energy gap defined as the midpoint between the peak absorption and emission energy, q is the charge of an electron, m is the mass of an electron, ϵ_0 is the permittivity of free space and η is the refractive index. The oscillator strength (f_{12}) is then estimated by integrating the molar absorption coefficient $\int_{S_1} \varepsilon(E)\,dE$ consistent with a single electronic state contributing to the absorption spectrum (equation (3)).

$$f_{12} = \frac{2\epsilon_0 mc\eta}{\pi\hbar q^2} \frac{1,000}{N_A \log_{10} e} \int_{S_1} \varepsilon(E)\,dE \tag{3}$$

https://doi.org/10.1038/s41557-024-01464-6

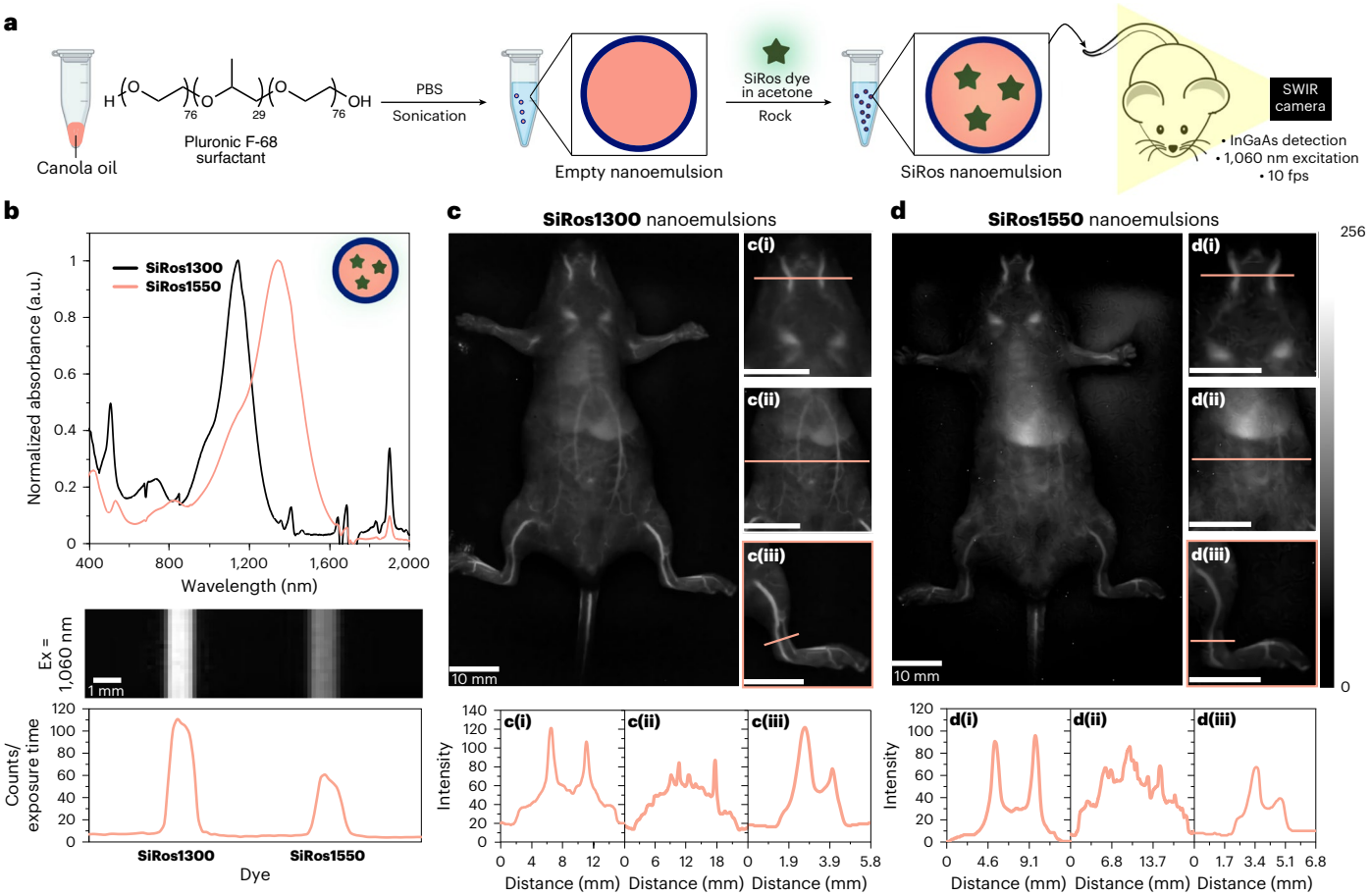

Fig. 5 | Preparation of SiRos nanoemulsions and visualization in vivo via intravenous injection. a, Representative nanoemulsion preparation beginning with canola oil emulsification using a Pluronic F-68 surfactant in PBS, followed by loading of the nanoemulsion with dye via rocking of the solution. **b**, Top: absorption spectra of **SiRos1300** and **SiRos1550** nanoemulsions in PBS. Bottom: InGaAs camera comparative brightness imaging of **SiRos1300** and **SiRos1550** nanoemulsions at 56.3 μM and 226 μM respectively (three-times dilution of intravenous injected samples), excited at 1,060 nm. A representative image with 1,060 nm excitation is shown, and the plot represents quantification of the intensities calibrated to counts/exposure time. **c**,**d**, In vivo fluorescent images of **SiRos1300** (**c**) and **SiRos1550** (**d**) nanoemulsions following tail vein injection along with cross-sectional intensities depicted in **c(i–iii)** or **d(i–iii)** below each figure. These samples are illuminated with diffuse 1,060 nm excitation and collected using an InGaAs camera equipped with a 1,300 nm longpass filter.

However, the oscillator strength of emission is substantially diminished, suggesting that a large number of dark emissive states contribute to the observed photophysics. An estimate of the number of emissive states is given by degeneracy ratio ($\frac{g_2}{g_1} = \frac{f_{12}}{f_{21}}$) of S_1 states to S_0 states, which goes as high as 270 for **SiRos1700** (ref. 48). The degeneracy ratio is dramatically increased compared with the typical g_2/g_1 of 2–3 observed for polymethine dyes[41]. This number cannot be taken as a precise estimate of the number of electronic configurations near the bandgap, yet it strongly suggests potential mixing of singlet and triplet excited states as the S_1–S_0 gap closes, resulting in lengthening of the fluorescent lifetimes and perhaps protecting the excited state from direct internal conversion to the ground state. Computation using B3LYP/6-311 G(*d*,*p*)-level theory shows that the energy gap between S_1 and T_2 is very small: 0.09 eV, 0.04 eV and 0.05 eV for **SiRos1300**, **SiRos1550** and **SiRos1700**, respectively (Supplementary Table 3 and Supplementary Fig. 18). Increasing $n \rightarrow \pi^*$ character in **SiRos1700** could also account for increasing lifetimes, diminished transition dipole moment and stronger coupling to triplet states, as suggested by the lifetime data.

Geometry optimizations and time-dependent density functional theory computations

Time-dependent density functional theory calculations were conducted for **SiRos1300**, **SiRos1550** and **SiRos1700** at the B3LYP/6-311g(*d*,*p*) level of theory[49–51] using Gaussian 16 software[52], with CH_2Cl_2 as an implicit solvent (Fig. 4 and Supplementary Table 4). The computationally predicted trend in vertical transition energy is consistent with the experimental $\lambda_{abs}{}^{max}$ trend in CH_2Cl_2, that is, **SiRos1300** < **SiRos1550** < **SiRos1700**. Analysis of the frontier molecular orbitals shows distribution of the HOMO is primarily localized on the indolizine donors and auxiliary DMA donors, with less distribution on the core of the chromophore. The delocalization of the HOMO across the auxiliary DMA donors indicates a strong contribution of these donors to the π-system and thus a strong effect on the vertical transition energy. The LUMO orbital distribution shows the orbital coefficients are spread primarily across the core of the chromophore and somewhat across the indolizine donors, with no appreciable contribution from the DMA groups. This movement of the orbital distribution between the HOMO and LUMO indicates some charge transfer character for these materials, and could explain the lower molar absorptivity compared with $\pi \rightarrow \pi^*$ systems such as cyanines, which demonstrate exceptional HOMO/LUMO overlap. The observed charge transfer-like character is also consistent with the experimental observation in switching between non-polar aprotic (CH_2Cl_2) and polar aprotic (CH_3CN) solvents, as the absorption broadens and the molar absorptivity decreases in CH_3CN compared with CH_2Cl_2 (Supplementary Fig. 2 and Table 1). **SiRos1550** and **SiRos1700** also have much higher energy transitions (oscillator strengths > 0.10):

675 nm for **SiRos1550**, and 917 nm and 648 nm for **SiRos1700** (Supplementary Table 4). These transitions are noticeable in the absorption spectrum of the dyes in CH_2Cl_2 as the lowest energy feature of **SiRos1700** is broadened, which is consistent with the computationally predicted transition at 917 nm. **SiRos1700** also has a broad feature near 700 nm, which is consistent with the computationally predicted transition at 648 nm. Similarly, **SiRos1550** has a transition around 800 nm that is consistent with the computationally predicted transition at 675 nm.

Fluorophore chemical stability

Dye stability towards a variety of nucleophiles was studied with **SiRos1300** in CH_3CN solution by measuring the remaining absorption of the dye at regular time intervals for each condition (Supplementary Fig. 19). The absorption of **SiRos1300** was observed to rapidly decay, with a complete loss of the fluorophore absorption signal before a measurement could be taken in the presence of small anionic nucleophiles (present at 10× concentration with respect to **SiRos1300**) including OH^- (K^+ counter ion), F^- (Bu_4N^+ counter ion) and CN^- (Bu_4N^+ counter ion; see Methods for experimental details). In a 10% H_2O/CH_3CN solution stored under ambient conditions, **SiRos1300** was observed to maintain ~85% of its initial absorption over the course of a week, which indicates that anionic nucleophiles promote faster decay of the fluorophore absorption signal compared to neutral nucleophiles. This coincides with the reasonable stability of **SiRos1300** in large quantities of H_2O, but nearly instantaneous decay of the absorption signal in the presence of the KOH.

In vivo imaging experiments

Canola-oil-based nanoemulsions were investigated to allow for prolonged in vivo imaging. Nanoemulsions were made by emulsifying canola oil using a Pluronic F-68 surfactant in phosphate-buffered saline (Fig. 5a)[53]. The nanoemulsions were subsequently loaded with **SiRos1300** or **SiRos1550** dissolved in acetone by rocking the mixture for at least 1 h. Note that **SiRos1700** was excluded from the imaging experiments as the range of the SWIR camera utilized herein does not capture the bulk of the emission. The SWIR-emissive nanoemulsions were washed via three successive spins through a centrifugal filter (molecular weight cut-off = 10,000 Da, 4,000 r.p.m. or 3,739 × *g*), and then characterized by absorption spectroscopy, SWIR camera emission and dynamic light scattering (Fig. 5b and Supplementary Fig. 21) before in vivo use. **SiRos1300** nanoemulsions were an average size of 260 nm with a polydispersity index of 0.44, whereas **SiRos1550** nanoemulsions were an average size of 194 nm with a polydispersity index of 0.27. Absorption spectra of the **SiRos1300**- and **SiRos1550**-loaded nanoemulsions demonstrate very similar features to the absorption of the dyes in organic solvent (Fig. 3), indicating single molecule behaviour of the fluorophores in the nanoemulsions (Fig. 5b, top). **SiRos1300** nanoemulsions were observed to be roughly twice as bright as **SiRos1550** nanoemulsions under the same imaging conditions (Fig. 5b, bottom).

SiRos1300 and **SiRos1550** nanoemulsions both demonstrate excellent spatial resolution, a characteristic feature in SWIR fluorescence imaging (Fig. 5c,d and Supplementary Fig. 22). Both nanoemulsions are observed to distribute throughout the entire circulatory system shortly after tail vein injection, with well-defined resolution of the mouse vasculature in regions including the abdomen, jugular vein and femoral artery. The cross-sectional intensities are shown in Fig. 5c,d for **SiRos1300** and **SiRos1550**, respectively. **SiRos1300** is observed to produce greater peak signal intensities than **SiRos1550** along the jugular (~120 a.u. versus ~100 a.u.) and femoral artery (~120 a.u. versus ~70 a.u) cross-sections, whereas both fluorophores produce comparable peak signal intensities along the abdominal cross-section (~80 au). Furthermore, mice injected with both nanoemulsions displayed a detectable signal two weeks after injection.

With their low-energy emission, **SiRos1300**, **SiRos1550** and **SiRos1700** are primed to capitalize on the advantages of the SWIR region including: (1) imaging in the high-contrast regions of 1,400–1,600 nm; (2) imaging at greater depths; and (3) expanding multiplexed capabilities. We have demonstrated the potential for each of these avenues through capillary imaging experiments with **SiRos1300** and **SiRos1550**. Both **SiRos1300** and **SiRos1550** display robust signal when imaging with 1,400 nm and 1,500 nm longpass filters (Supplementary Fig. 23). To evaluate the impact of using low-energy wavelengths on depth penetration, we equalized the brightness of **SiRos1300** and **SiRos1550**, and three other fluorophores with higher-energy λ_{emis}^{max}: JuloChrom5 (872 nm), Chrom7 (996 nm), JuloFlav7 (1,088 nm)[54]. We imaged these five capillaries at varying depths of 1% Intralipid—a common medium used as a tissue phantom (Extended Data Fig. 1; Supplementary Figs. 24 and 25)[55]. Capillaries with longer-wavelength-emitting dyes can be resolved at deeper depths. Using a 1,400 nm longpass filter, only **SiRos1550** can be resolved at 4 mm depth, with **SiRos1300**, JuloFlav7, Chrom7 and JuloChrom5 being resolved at 3.5 mm, 3 mm, 2.5 mm and 2 mm, respectively. Similar findings are seen using a 1,500 nm longpass filter, with only **SiRos1300** and **SiRos1550** being resolvable at 4 mm depth. This is consistent with Intralipid experiments of previous works demonstrating superior depth penetration and resolution using longer-wavelength emitters[56]. Finally, an important advantage of the SWIR region is expanding the spectral window applicable for imaging through tissue, facilitating multicolour experiments. The SiRos dyes expand to regions previously unreached by biocompatible fluorophores. **SiRos1300** is able to be multiplexed alongside JuloChrom5 and Chrom7 (Supplementary Fig. 26). Due to limitations in excitation lasers, we were unable to increase the number of channels used for multiplexing, yet this should be able to be achieved with technology advances. The SiRos dyes demonstrate the importance of the interplay between technology and probe development, with these dyes surpassing the optimized excitation and emission ranges of current SWIR imaging set-ups.

Conclusion

Here we design and synthesize a series of SiRos fluorophores and characterize their photophysical properties. **SiRos1300**, **SiRos1550** and **SiRos1700** have λ_{emis}^{max} of 1,300 nm, 1,557 nm and 1,700 nm, along with fluorescence quantum yields of 0.0056%, 0.0025% and 0.0011%, respectively (all in CH_2Cl_2). Photoluminescent lifetimes in the picosecond regime were observed for the series, along with an inverse trend in lifetime and emission energy, in which **SiRos1700** > **SiRos1550** > **SiRos1300**. The observed photoluminescent lifetime trend is attributed to potential mixing of the singlet and triplet excited states as the optical gap of the fluorophores decreases. Time-dependent density functional theory analysis of the fluorophores matches trends observed in the dye series in which **SiRos1700** > **SiRos1550** > **SiRos1300** for absorption wavelength and vertical transition. The frontier molecular orbitals indicate partial charge transfer behaviour, which is observed experimentally as the absorption width broadens and the molar absorptivity decreases when switching from non-polar aprotic (CH_2Cl_2) to polar aprotic solvents (CH_3CN). In vivo SWIR imaging experiments were conducted using **SiRos1300** and **SiRos1550** in canola oil-based nanoemulsions. The formulations exhibited full circulatory distribution and high-resolution imaging of mouse vasculature in the femoral arteries, abdominal cavity and jugular veins. Overall, this work illustrates design principles for future long wavelength emitting SWIR fluorophores. Future efforts are focused on designing water soluble fluorophores and higher quantum yield fluorophores in the ESWIR region. Furthermore, fluorophores emitting in the midwave infrared (3,000–5,000 nm) region are being pursued based on these design principles.

Online content

Any methods, additional references, Nature Portfolio reporting summaries, source data, extended data, supplementary information, acknowledgements, peer review information; details of author contributions and competing interests; and statements of data and code availability are available at https://doi.org/10.1038/s41557-024-01464-6.

References

1. Li, H., Wang, X., Li, X., Zeng, S. & Chen, G. Clearable shortwave-infrared-emitting $NaErF_4$ nanoparticles for noninvasive dynamic vascular imaging. *Chem. Mater.* **32**, 3365–3375 (2020).
2. Barton, J. B., Demro, J. C., Gasparian, G. & Lange, M. *Performance of an Uncooled Camera Utilizing an SWIR InGaAs 256×256 FPA for Imaging in the 1.0 μm – 1.7 μm Spectral Band*. Defense Public Release: Technical Report, ADA399438 (US Department of Defense, 1998).
3. Chinnathambi, S. & Shirahata, N. Recent advances on fluorescent biomarkers of near-infrared quantum dots for in vitro and in vivo imaging. *Sci. Technol. Adv. Mater.* **20**, 337–355 (2019).
4. Hong, G., Antaris, A. L. & Dai, H. Near-infrared fluorophores for biomedical imaging. *Nat. Biomed. Eng.* **1**, 0010 (2017).
5. Owens, E. A., Henary, M., El Fakhri, G. & Choi, H. S. Tissue-specific near-infrared fluorescence imaging. *Acc. Chem. Res.* **49**, 1731–1740 (2016).
6. Tian, C. & Burgess, K. Flavylium and silylrhodapolymethines In excitation multiplexing. *ChemPhotoChem* **5**, 702–704 (2021).
7. Usama, S. M. & Burgess, K. Hows and whys of tumor-seeking dyes. *Acc. Chem. Res.* **54**, 2121–2131 (2021).
8. Wang, R., Li, X. & Yoon, J. Organelle-targeted photosensitizers for precision photodynamic therapy. *ACS Appl. Mater. Interfaces* **13**, 19543–19571 (2021).
9. Liu, D. et al. Xanthene-based NIR-II dyes for in vivo dynamic imaging of blood circulation. *J. Am. Chem. Soc.* 17136–17143 (2021).
10. Kim, B., Kim, H., Kim, S. & Hwang, Y. R. A brief review of non-invasive brain imaging technologies and the near-infrared optical bioimaging. *Appl. Microsc.* **51**, 9 (2021).
11. Wen, H. & Bellotti, E. Numerical study of the intrinsic recombination carriers lifetime in extended short-wavelength infrared detector materials: a comparison between InGaAs and HgCdTe. *J. Appl. Phys.* **119**, 205702 (2016).
12. Vittadello, L. et al. NIR–to–NIR Imaging: extended excitation up to 2.2 um using harmonic nanoparticles with a Tunable hIGh EneRgy (TIGER) widefield microscope. *Nanomaterials* **11**, 3193 (2021).
13. Sordillo, D. C., Sordillo, L. A., Sordillo, P. P., Shi, L. & Alfano, R. R. Short wavelength infrared optical windows for evaluation of benign and malignant tissues. *J. Biomed. Opt.* **22**, 45002 (2017).
14. Carr, J. A. et al. Absorption by water increases fluorescence image contrast of biological tissue in the shortwave infrared. *Proc. Natl Acad. Sci. USA* **115**, 9080 (2018).
15. Shapiro, A. et al. Tuning optical activity of IV–VI colloidal quantum dots in the short-wave infrared (SWIR) spectral regime. *Chem. Mater.* **28**, 6409–6416 (2016).
16. Shi, X. et al. Zn-doping enhances the photoluminescence and stability of PbS quantum dots for in vivo high-resolution imaging in the NIR-II window. *Nano Res.* **13**, 2239–2245 (2020).
17. Li, Y. et al. Novel NIR-II organic fluorophores for bioimaging beyond 1550 nm. *Chem. Sci.* **11**, 2621–2626 (2020).
18. Sun, C. et al. *J*-Aggregates of cyanine dye for NIR-II in vivo dynamic vascular imaging beyond 1500 nm. *J. Am. Chem. Soc.* **141**, 19221–19225 (2019).
19. Carr, J. A. et al. Shortwave infrared fluorescence imaging with the clinically approved near-infrared dye indocyanine green. *Proc. Natl Acad. Sci. USA* **115**, 4465–4470 (2018).
20. Khan, Z. & Sekar, N. Far-red to NIR emitting xanthene-based fluorophores. *Dyes Pigm.* **208**, 110735 (2022).
21. Rathnamalala, C. S. L. et al. Donor–acceptor–donor NIR II emissive rhodindolizine dye synthesized by C–H bond functionalization. *J. Org. Chem.* **84**, 13186–13193 (2019).
22. Chatterjee, S. et al. SWIR emissive RosIndolizine dyes with nanoencapsulation in water soluble dendrimers. *RSC Adv.* **11**, 27832–27836 (2021).
23. Chatterjee, S. et al. Design and synthesis of rhodIndolizine dyes with improved stability and shortwave infrared emission up to 1250 nm. *J. Org. Chem.* **87**, 11319 (2022).
24. Grimm, J. B., Brown, T. A., Tkachuk, A. N. & Lavis, L. D. General synthetic method for Si-fluoresceins and Si-rhodamines. *ACS Cent. Sci.* **3**, 975–985 (2017).
25. Best, Q. A., Sattenapally, N., Dyer, D. J., Scott, C. N. & McCarroll, M. E. pH–Dependent Si-fluorescein hypochlorous acid fluorescent probe: spirocycle ring-opening and excess hypochlorous acid-induced chlorination. *J. Amer. Chem. Soc.* **135**, 13365–13370 (2013).
26. Huang, Y. L., Walker, A. S. & Miller, E. W. A photostable silicon rhodamine platform for optical voltage sensing. *J. Am. Chem. Soc.* **137**, 10767–10776 (2015).
27. Zheng, Q. et al. Rational design of fluorogenic and spontaneously blinking labels for super-resolution Imaging. *ACS Cent. Sci.* **5**, 1602–1613 (2019).
28. Kushida, Y., Nagano, T. & Hanaoka, K. Silicon-substituted xanthene dyes and their applications in bioimaging. *Analyst* **140**, 685–695 (2015).
29. Liu, M. H., Zhang, Z., Yang, Y. C. & Chan, Y. H. Polymethine-based semiconducting polymer dots with narrow-band emission and absorption/emission maxima at NIR-II for bioimaging. *Angew. Chem. Int. Ed.* **60**, 983–989 (2021).
30. Yang, Y. et al. Counterion-paired bright heptamethine fluorophores with NIR-II excitation and emission enable multiplexed biomedical imaging. *Angew. Chem. Int. Ed.* **61**, e202117436 (2022).
31. Ando, N., Soutome, H. & Yamaguchi, S. Near-infrared fluorescein dyes containing a tricoordinate boron atom. *Chem. Sci.* **10**, 7816–7821 (2019).
32. Lei, Z. et al. Synthesis of sterically protected xanthene dyes with bulky groups at C-3′ and C-7′. *J. Org. Chem.* **80**, 11538–11543 (2015).
33. McNamara, L. E. et al. Indolizine-squaraines: NIR fluorescent materials with molecularly engineered Stokes shifts. *Chem. Eur. J.* **23**, 12494–12501 (2017).
34. Ndaleh, D. et al. Shortwave infrared absorptive and emissive pentamethine-bridged indolizine cyanine dyes. *J. Org. Chem.* **86**, 15376–15386 (2021).
35. Deng, F. & Xu, Z. Heteroatom-substituted rhodamine dyes: structure and spectroscopic properties. *Chin. Chem. Lett.* **30**, 1667–1681 (2019).
36. Waggener, W. C. Absorbance of liquid water and deuterium oxide between 0.6 and 1.8 microns comparison of absorbance and effect of temperature. *Anal. Chem.* **30**, 1569–1570 (1958).
37. Wang, S. et al. Anti-quenching NIR-II molecular fluorophores for in vivo high-contrast imaging and pH sensing. *Nat. Commun.* **10**, 1058 (2019).
38. Cosco, E. D. et al. Flavylium polymethine fluorophores for near- and shortwave infrared imaging. *Angew. Chem. Int. Ed.* **56**, 13126–13129 (2017).
39. Semonin, O. E. et al. Absolute photoluminescence quantum yields of IR-26 Dye, PbS, and PbSe quantum dots. *J. Phys. Chem. Lett.* **1**, 2445–2450 (2010).
40. Kratkiewicz, K., Manwar, R., Zhou, Y., Mozaffarzadeh, M. & Avanaki, K. Technical considerations in the Verasonics research ultrasound platform for developing a photoacoustic imaging system. *Biomed. Opt. Express* **12**, 1050–1084 (2021).

41. Friedman, H. C. et al. Establishing design principles for emissive organic SWIR chromophores from energy gap laws. *Chem* **7**, 3359–3376 (2021).
42. Atallah, T. L. et al. Decay-associated Fourier spectroscopy: visible to shortwave infrared time-resolved photoluminescence. *Spectra. J. Phys. Chem. A* **123**, 6792–6798 (2019).
43. Caspar, J. V., Sullivan, B. P., Kober, E. M. & Meyer, T. J. Application of the energy gap law to the decay of charge transfer excited-states. Solvent effects. *Chem. Phys. Lett.* **91**, 91–95 (1982).
44. Siebrand, W. Radiationless transitions in polyatomic molecules. I. Calculation of Franck–Condon factors. *J. Chem. Phys.* **46**, 440–447 (1967).
45. Siebrand, W. Radiationless transitions in polyatomic molecules. II. Triplet-ground-state transitions in aromatic hydrocarbons. *J. Chem. Phys.* **47**, 2411–2422 (1967).
46. Caspar, J. V. & Meyer, T. J. Application of the energy gap law to nonradiative, excited-state decay. *J. Phys. Chem.* **87**, 952–957 (1983).
47. Maillard, J. et al. Universal quenching of common fluorescent probes by water and alcohols. *Chem. Sci.* **12**, 1352–1362 (2020).
48. Zheng, L., Polizzi, N. F., Dave, A. R., Migliore, A. & Beratan, D. N. Where Is the electronic oscillator strength? Mapping oscillator strength across molecular absorption. *Spectra. J. Phys. Chem. A* **120**, 1933–1943 (2016).
49. Frisch, M. J., Pople, J. A. & Binkley, J. S. Self-consistent molecular orbital methods 25. Supplementary functions for Gaussian basis sets. *J. Chem. Phys.* **80**, 3265–3269 (1983).
50. Lee, C., Yang, W. & Parr, R. G. Development of the Colle–Salvetti correlation-energy formula into a functional of the electron density. *Phys. Rev. B* **37**, 785–789 (1988).
51. Becke, A. D. Density-functional thermochemistry. III. The role of exact exchange. *J. Chem. Phys.* **98**, 5648–5652 (1993).
52. Frisch, M. J. et al. *Gaussian 16, Revision A.03* (Gaussian, Inc, 2016).
53. Day, R. A., Estabrook, D. A., Logan, J. K. & Sletten, E. M. Fluorous photosensitizers enhance photodynamic therapy with perfluorocarbon nanoemulsions. *Chem. Commun.* **53**, 13043–13046 (2017).
54. Cosco, E. D. et al. Bright chromenylium polymethine dyes enable fast, four-color in vivo imaging with shortwave infrared detection. *J. Am. Chem. Soc.* **143**, 6836–6846 (2021).
55. Flock, S. T., Jacques, S. L., Wilson, B. C., Star, W. M. & van Gemert, M. J. Optical properties of Intralipid: a phantom medium for light propagation studies. *Lasers Surg Med* **12**, 510–519 (1992).
56. Wang, F. et al. In vivo non-invasive confocal fluorescence imaging beyond 1,700 nm using superconducting nanowire single-photon detectors. *Nat. Nanotechnol.* **17**, 653–660 (2022).
57. Rurack, K. & Spieles, M. Fluorescence quantum yields of a series of red and near-infrared dyes emitting at 600–1000 nm. *Anal. Chem.* **83**, 1232–1242 (2011).
58. Lu, L. et al. NIR-II bioluminescence for in vivo high contrast imaging and in situ ATP-mediated metastases tracing. *Nat. Commun.* **11**, 4192 (2020).
59. Ishchenko, A. A. et al. Electronic structure and spectral-fluorescent properties of thiopyrylo-4-tricarbocyanine laser dyes. *Opt. Spectrosc.* **129**, 926–934 (2021).

Methods

General synthetic information

We purchased 2-bromo-4-chloro-1-iodobenzene and 2-bromo-4-chlorobenzaldehyde from 1PlusChem, dichlorobis(2-ethylhexyl)silane from Gelest, and DSPE-mPEG2000 from AaronChem. Common reagents and solvents were purchased from Ambeed, Tokyo Chemical Industry, Sigma-Aldrich, Acros Organics and Thermo Fischer Scientific, and were used without further purification. Thin layer chromatography was conducted using Sorbtech Silica XHL TLC plates (glass-backed support; thickness = 250 µm) and visualized with an ultraviolet lamp. Flash column chromatography was performed using a Teledyne CombiFlash Rf+ system. The silica gel cartridges were purchased from Luknova SuperSep (FC003012, 50 µm).

Synthesis

Detailed synthetic procedures and characterization data are provided in the Supplementary Information.

Characterization information

^{1}H and ^{13}C {^{1}H} NMR spectra were recorded on Bruker Ascend 300 (300 MHz) and 400 (400 MHz) spectrometers using deuterated solvents. *J* values are expressed in hertz and chemical shifts are in parts per million, using residual solvent as an internal standard ($CDCl_3$ at 7.26 ppm, CD_2Cl_2 at 5.32 ppm and $(CD_3)_2CO$ at 2.05 ppm). Singlet (s), doublet (d), doublet of doublets (dd), triplet (t), multiplet (m), multiple signals (ms), broad (br) and apparent (ap) are designated as ^{1}H-NMR multiplicity patterns. High-resolution mass spectra were obtained with quadrupole time-of-flight, high-resolution-mass-spectrometry-utilizing nanospray ionization. The mass analyser was set to the 200–2,000 Da range. Infrared spectra were recorded with an Agilent Cary 660 attenuated total reflection-Fourier-transform infrared spectrometer. All of the absorption profiles were recorded on a Cary 5000 ultraviolet–visible–near-infrared spectrophotometer set to the double beam mode, with all dyes at a concentration of 1×10^{-5} M. All fluorescence spectra were conducted with a dye concentration of 1×10^{-5} M. The fluorescence quantum yield (referenced to IR-1061 at 0.32% in CH_2Cl_2)[38] of **SiRos1300** was recorded using a HORIBA QuantaMaster 8075–21 spectrofluorometer with xenon lamp excitation and a liquid-nitrogen-cooled InGaAs solid-state detector, and was determined to be 0.0056% in CH_2Cl_2 using equation (4) below:

$$\Phi_{\text{sample}} = \Phi_{\text{standard}} \times \frac{E_{\text{sample}}}{E_{\text{standard}}} \times \frac{A_{\text{standard}}}{A_{\text{sample}}} \times \frac{\eta^2_{\text{sample}}}{\eta^2_{\text{standard}}} \quad (4)$$

where E is the integrated emission counts; A is 1×10^{-A}, where the superscript A is the absorbance at the excitation wavelength; η is the refractive index of the solvent used; and Φ denotes the fluorescence quantum yield. The steady-state emission spectra shown in Fig. 3 and Supplementary Figs. 4–13 were acquired using a HORIBA Fluorolog-QM, which is the fourth generation of the Fluorolog spectrofluorometer (the set-up shown in Supplementary Fig. 1). A 980 nm diode-pumped solid-state (2 W) laser was used as the excitation source, and was mounted to the front panel of the Fluorolog-QM's sample tray. A HORIBA liquid-nitrogen-cooled solid state detector (DSS) InAs detector was used to detect the emission through a monochromator (350 mm focal length) with a ruled diffraction grating (600 grooves per millimetre, blazed at 1.25 µm), a scanning increment of 2 nm and an emission bandpass of 30 nm. To increase the detector's sensitivity, a lock-in amplifier with the liquid-nitrogen-cooled InAs detector was used. A transistor–transistor logic output signal (27 Hz) from the chopper control was used as the reference signal to the lock-in-amplifier control, and also as the trigger signal to the laser control to electrically chop the 980 nm diode-pumped solid-state laser. The time constant of the lock-in amplifier was set to 100 ms, and the detector integration time was 0.3 s. The fluorescence quantum yields of **SiRos1550** and **SiRos1700** were subsequently referenced to the obtained value of 0.0056 ± 0.0007% for **SiRos1300**. As the equation for relative Φ_F (equation (4)) includes the multiplication and division of measured values, the relative standard deviation (RSD) of each Φ_F is calculated by taking the square root of the sum of the RSDs of each of the measured values using equation (5) below:

$$\text{RSD}_{\Phi S} = \sqrt{\text{RSD}_{\Phi R}{}^2 + \text{RSD}_{\text{AbsR}}{}^2 + \text{RSD}_{\text{AbsS}}{}^2 + \text{RSD}_{\text{EmisS}}{}^2 + \text{RSD}_{\text{EmisR}}{}^2} \quad (5)$$

The RSD for the Φ_F of the reference ($\text{RSD}_{\Phi R}$) is well-documented in the literature to be 0.32% ± 0.04% for IR-1061, which generates an $\text{RSD}_{\Phi R}$ of 12.5%[38]. The RSDs for the absorption values of the reference (RSD_{AbsR}) and sample (RSD_{AbsS}) were determined by taking a sample of **SiRos1300** with an absorption value comparable to those used in the emission experiments (~0.2–0.3), and measuring the absorption at 980 nm ten times. The absorption was observed to be 0.258 ± 0.004, generating an RSD of 1.63%. The RSD of the emission experiments was determined by calculating the s.d. of a blank sample (s.d. = ±0.0266 counts) and using this to determine the theoretical upper and lower bounds for the integrated emission counts. To do this, the s.d. was multiplied by the number of points collected in each emission experiment to determine how much higher (or lower) the integrated emission intensity would be if every point was 1 s.d. higher (or lower) than the measured value. The upper/lower bounds determined using this method are greater than what would likely be observed experimentally because normal, random variations in measurements typically cancel each other out; however, they provide a logical means for error propagation herein. In this way, the difference in the upper/lower bounds of emission intensity could be divided by the integrated emission intensity to obtain the RSD of the reference ($\text{RSD}_{\text{EmisR}}$) and sample ($\text{RSD}_{\text{EmisS}}$). With the RSD of each measurement determined, the RSD for each Φ_F experiment could be calculated and the s.d. determined (Supplementary Table 1). The recorded emission spectra were smoothed with a LOESS function, and raw data and fitted data are overlaid in Supplementary Figs. 5–7 and 11–13. Solvent selection is key for SWIR emission spectroscopy as some solvents demonstrate less and/or weaker absorption features than others, and thus have less intense dips resulting in less disrupted spectra. Although CH_2Cl_2 is not the ideal solvent for emission spectroscopy due to the intense absorption feature at 1,700 nm, it was selected due to its consistency across the literature. To correct for solvent reabsorption in the fluorescence emission spectrum of the SiRos dyes, regions of the spectra that were observed to have substantial portions of the integrated emission overlapping with solvent absorption were removed and replaced by a straight line (Supplementary Fig. 8–10). These regions included 1,300–1,550 nm, 1,580–1,780 nm and 1,800–1,950 nm. The 1,580–1,780 nm region in **SiRos1700** was replaced by straight line segments to extrapolate the peak emission for the fluorophore based on the mirror image of the absorption spectra. To do so, the *x*-axis of the absorption spectra was plotted in reverse energy, and the emission and absorption spectra were overlaid; points were added every 20 nm to generate a curve matching that of the absorption spectra. This was necessary to extrapolate the emission maxima of **SiRos1700**.

Photoluminescent lifetimes

Photoluminescence lifetimes for **SiRos1300**, **SiRos1550** and **SiRos1700** were recorded using a home-built, all-reflective epifluorescence set-up[42]. A pulsed 785 nm laser was used as an excitation source and the emission was collected and filtered with a 90:10 beam splitter; the appropriate excitation filters were then reflectively coupled into a single-mode fibre (F–SMF-28-C-10FC, Newport) and detected using a superconducting nanowire single-photon detector (Quantum Opus One)[42,54,60]. Given the short photoluminescent lifetimes of the dyes, the lifetimes were fit with a convolution of the instrument response function as well as an exponential function. To determine the lifetime (or decay rate, *k*) for each of the time-correlated single-photon counting

traces, each curve was fit to a convolution of the sum of two gaussians with a single exponential decay as shown in equation (6) below:

$$I(t) = \frac{I_0}{2} e^{-k\left((t-t_0)-\frac{\sigma_1^2 k}{2}\right)}\left(1+\mathrm{erf}\left(\frac{(t-t_0)-\sigma_2^2 k}{\sqrt{2}\sigma}\right)\right) + \frac{aI_0}{2} e^{-k\left((t-t_0-t_1)-\frac{\sigma_2^2 k}{2}\right)}\left(1+\mathrm{erf}\left(\frac{(t-t_0-t_1)-\sigma_2^2 k}{\sqrt{2}\sigma_2}\right)\right) \quad (6)$$

where the width of the sum of the gaussians (σ_1 and σ_2), the time offset (t_0) between the two gaussians, and the amplitude scale (a) were determined using the instrument response function (IRF) measured as the backscatter off of a cuvette with solvent (that is CH_2Cl_2) without longpass filters. The initial peak amplitude (I_0), the rate (a), and t_0 are free-fitting parameters, whereas the time offset (t_1) and the IRF widths (σ_1 and σ_2) were fixed variables. A conservative error of ± 1 ps (the instrument resolution) was used for the lifetimes. The IRF fit values used in the above equation are: σ_1= 40.7, σ_2 = 66.6, t_1 = 82.7 and a = 0.25.

Fluorophore stability

All fluorophore stability studies were conducted using **SiRos1300** (2×10^{-5} M) in anhydrous CH_3CN that was freshly distilled over CaH_2. All stability studies were conducted in triplicate to ensure reproducibility; the error bars found in the graphs are given as the s.d. of the percent-remaining absorption of the three trials at each respective time point (Supplementary Fig. 19). Nucleophiles including OH^-, F^- and CN^- were added to the **SiRos1300** solution from a stock solution to yield a final nucleophile concentration of 2×10^{-4} M (10× with respect to **SiRos1300**). The OH^- stock solution consisted of 6×10^{-2} M KOH in H_2O, and 10 µl of this solution was added to 3 ml of 2×10^{-5} M **SiRos1300** in CH_3CN to yield an OH^- concentration of 2×10^{-4} M. Identical concentrations and volumes were used for the F^- and CN^- nucleophiles with tetrabutylammonium counter ions (used to impart organic solubility), except the stock solution was made using anhydrous CH_3CN instead of H_2O. The stability of **SiRos1300** to neutral water was studied in 10% H_2O/CH_3CN as higher concentrations of H_2O were observed to impact the solubility of the hydrophobic fluorophore. The remaining absorption was tracked over the course of a week as **SiRos1300** was observed to be quite stable to neutral water. Other nucleophiles including sodium acetate (NaOAc) and *n*-butylamine were observed to have slower absorption decay rates than OH^-, F^- and CN^- yet much faster than H_2O; 10× concentration of both NaOAc and *n*-butylamine yielded relatively slow absorption decay, so higher concentrations were used to generate stability curves on shorter time scales. The concentration of saturated NaOAc in CH_3CN has previously been determined to be 1.4×10^{-3} M, 70× that of **SiRos1300**, and was used as the nucleophile concentration herein[61]. For this, excess anhydrous NaOAc was added to a vial followed by roughly 5 ml of anhydrous CH_3CN. The solution was sonicated at 25 °C for 10 min, then 3 ml of this solution was added directly to a cuvette through a syringe filter containing the necessary amount of **SiRos1300** to yield a final concentration of 2×10^{-5} M and the absorption monitored over ~20 min; *n*-butylamine is freely soluble in CH_3CN and was used at a concentration of 2×10^{-3} M, 100 × with respect to **SiRos1300**; 3 ml of the *n*-butylamine solution was added directly to a cuvette containing the necessary amount of **SiRos1300** to yield a final concentration of 2×10^{-5} M and the absorption monitored over ~60 min.

Intralipid depth experiments

Intralipid depth experiments were conducted in 1% intralipid by first matching the five dyes **SiRos1550, SiRos1300**, **JuloFlav7**, **Chrom7** and **JuloChrom5** in CH_2Cl_2 by brightness within 1 mm diameter capillaries using a 1,300 nm, 1,400 nm or 1,500 nm longpass filter with an exposure time of 5 ms, 10 ms or 30 ms, respectively. The 0 mm depth images were acquired using the SWIR apparatus (described below) with the capillaries placed in a non-emissive square plastic container and submerged up to the brim with the intralipid solution. Intralipid solution was then added to the container until an additional 0.5 mm depth was formed over the capillaries, after which imaging was performed. This step was repeated up to a depth of 4 mm.

Animal procedures

Animal experiments were conducted in conformity with UCLA IACUC institutional guidelines (protocol no. ARC-2018-047). Non-invasive whole mouse imaging was performed on athymic nude female mice (5–7 weeks old), purchased from Charles River Laboratories. Mice were anaesthetized with inhaled isoflurane/oxygen set between 2 and 3%. Tail vein injections were performed with a catheter assembled from a 29-gauge needle from an insulin syringe connected through plastic tubing to a syringe prefilled with isotonic saline solution. The bevel of the needle was then inserted into the tail vein and secured using glue. The plastic tubing was then connected to an insulin syringe prefilled with the nanoemulsion suspension. All probes were filtered through a 0.45 µm syringe filter prior to intravenous injection; 200 µl of each formulation was injected intravenously. After injection of all formulations, the volume of the catheter was chased with saline to ensure full dosage.

SWIR imaging apparatus

An InGaAs camera (Allied Vision Goldeye G-032 Cool TEC2) was fitted with a C-mount camera lens (Kowa LM35HC-SW) and emission filters, and mounted vertically above the imaging workspace. The camera used a sensor temperature set point of −30 °C. The laser (LU1064DLD350-S70AN03; 35 W) output was coupled to a cube via a 600 nm core fibre-optic bundle (Lumics, LU_LWL0600_0720_220D1A1). The output from the fibre was fixed in an excitation cube (Thorlabs KCB1E), reflected off a mirror (Thorlabs BBE1-E03), and passed through (1) a positive achromat (Thorlabs AC254-050-AB-ML), (2) 1,300 nm short-pass filters (Edmund Optics no. 84-768) and (3) an engineered diffuser (Thorlabs ED1-S20-MD) to provide uniform illumination over the working area. The excitation flux was measured over the area of interest using a digital optical power and energy meter (Thorlabs PM100D). The camera and lasers were externally controlled and synchronized by delivering trigger pulses of 5 V transistor–transistor logic to the laser drivers and camera using a programmable trigger controller. The trigger controller uses pulses generated with an Atmel Atmega328 microcontroller unit and programmed using Arduino Nano Rev 3 MCU (A000005) in the Arduino integrated development environment. The imaging data were then transferred to a PC via a gigabit ethernet interface. For image acquisition, the toolbox of MATLAB programming environment is used in combination with a MATLAB script (CCDA V3, https://gitlab.com/brunslab/ccda) to preview and collect the required image data in 14-bit depth.

Image processing

Images were processed using the FIJI distribution of ImageJ. We applied laser-off background subtraction to all images (about 200 frames were taken at the beginning of every movie) and frames of interest were noted. Once the appropriate frames were chosen, the average of the frames (~50 frames) were obtained using the 'z-project' command. These averages were then compressed from 14-bit (0–14,800 brightness) to 8-bit (0–255 brightness) depth for display. These images are displayed in Supplementary Fig. 22.

Multiplexed imaging acquisition

To achieve excitation-synchronized imaging, a semi-automatic imaging algorithm implemented in MATLAB (as described above in the 'SWIR imaging apparatus' section) was combined with manual control of laser parameters through the individual laser modules and the programmed microcontroller unit. The camera captured the excitation-synchronized frames, which were then transferred to a personal computer via the GigE interface.

Reporting summary

Further information on research design is available in the Nature Portfolio Reporting Summary linked to this article.

Data availability

The datasets generated during and/or analysed during the current study are available in a public repository https://zenodo.org/records/10079855 and are also available from the corresponding authors on reasonable request. Further graphical data pertaining to photophysical properties, electrochemistry, photoluminescent lifetimes, computation, micelle photostability, nanoemulsions, in vivo imaging, synthetic procedures and NMR spectra are also available in the Supplementary Information. Raw data for animal experiments can be accessed on the BioImage archive #S-BIAD548. Source Data are provided with this paper.

References

60. Pengshung, M. et al. Silicon incorporation in polymethine dyes. *Chem. Commun.* **56**, 6110–6113 (2020).
61. Soleymani, J., Zamani-Kalajahi, M., Ghasemi, B., Kenndler, E. & Jouyban, A. Solubility of sodium acetate in binary mixtures of methanol, 1-propanol, acetonitrile, and water at 298.2 K. *J. Chem. Eng. Data* **58**, 3399–3404 (2013).

Acknowledgements

We thank the National Science Foundation (NSF; award no. 1757220 to W.E.M., D.N., A.K.S., N.I.H. and J.H.D.), the National Institute of Health (NIH; award no. 1R01EB027172 to E.M.S.), the Tobacco-Related Disease Research Program (TRDRP; award no. T32DT4847 to E.Y.L.), and the UCLA for the Dissertation Year Fellowship (I.L.) for their financial support. J.R.C. and H.C.F. would like to acknowledge National Science Foundation Career Award No. 1945572 and support from the Cottrell Award. This manuscript is based on work supported by the National Science Foundation Graduate Research Fellowship Program awarded to W.E.M. Any opinions, findings and conclusions or recommendations expressed in this material are those of the author(s) and do not necessarily reflect the views of the National Science Foundation. The funders had no role in study design, data collection and analysis, decision to publish or preparation of the manuscript. We would also like to acknowledge the late Douglas Hamm from HORIBA Scientific for his assistance in facilitating the fluorescence emission data acquisition in this study.

Author contributions

W.E.M. synthesized the intermediates and fluorophores herein and collected absorption, emission, cyclic voltammetry measurements of the fluorophores along with the computational data. E.Y.L. and I.L. conducted the in vivo and capillary imaging experiments. H.C.F. conducted the photoluminescent lifetime experiments. D.N. synthesized compound **6**. A.K.S. collected the emission spectrum and calculated the fluorescence quantum yield of **SiRos1300**. N.I.H. designed and supervised the fluorescence studies. B.Y. collected the fluorescence emission spectra for all fluorophores at HORIBA Scientific. J.R.C. designed and supervised the photoluminescent lifetime experiments. E.M.S. designed and supervised the in vivo and capillary imaging experiments. J.H.D. designed and supervised the design, synthesis and characterization of the fluorophores herein. W.E.M. wrote the initial draft of the manuscript and all authors assisted in editing subsequent drafts. All authors discussed the results and contributed to the paper.

Competing interests

W.E.M., D.N. and J.H.D. have a patent pending which includes the dyes studied herein, US Patent 20220370641A1. The remaining authors declare no competing interests.

Additional information

Extended data is available for this paper at https://doi.org/10.1038/s41557-024-01464-6.

Supplementary information The online version contains supplementary material available at https://doi.org/10.1038/s41557-024-01464-6.

Correspondence and requests for materials should be addressed to Ellen M. Sletten or Jared H. Delcamp.

Peer review information *Nature Chemistry* thanks Luke Lavis and the other, anonymous, reviewer(s) for their contribution to the peer review of this work.

https://doi.org/10.1038/s41557-024-01464-6

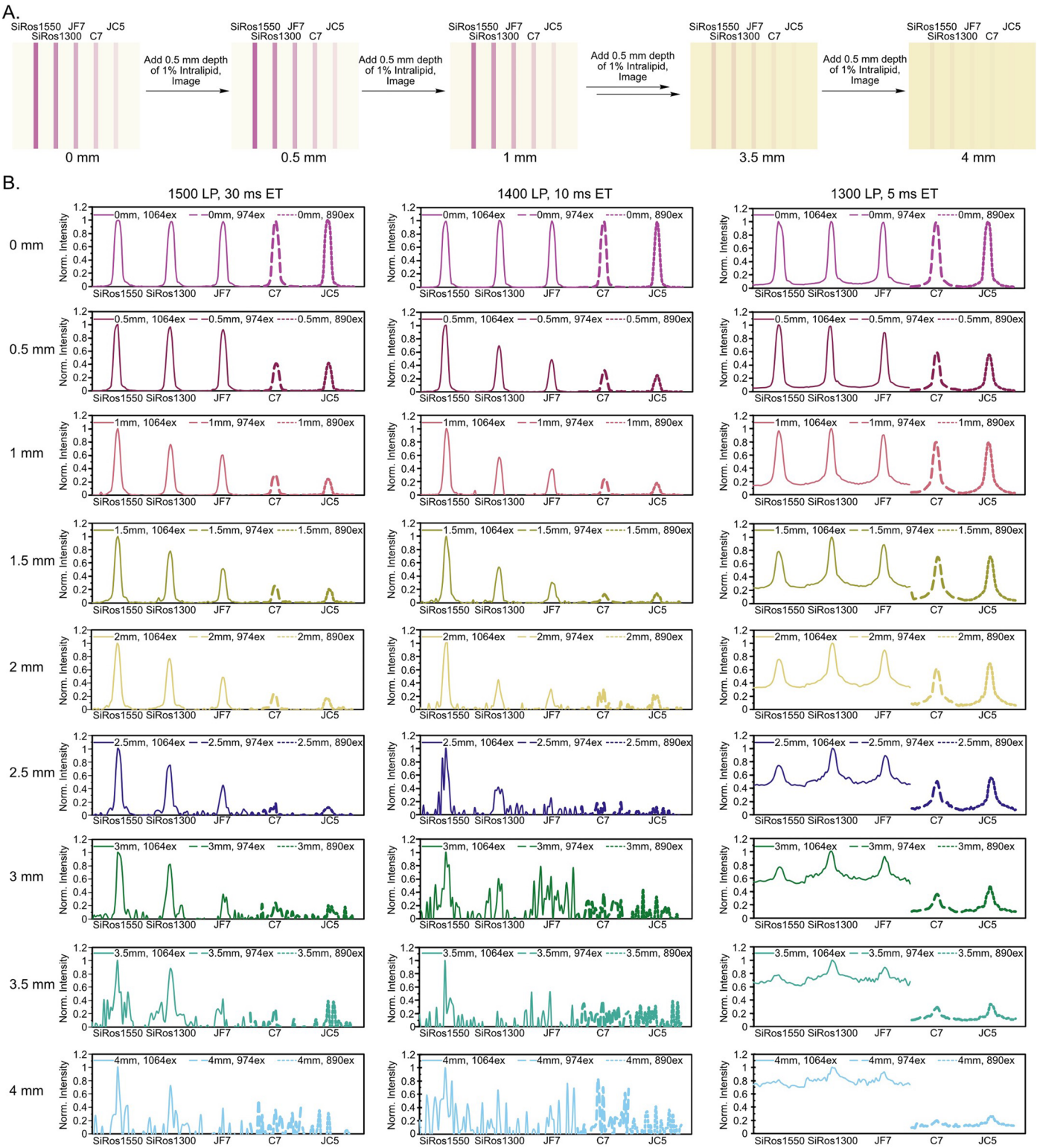

Extended Data Fig. 1 | Evaluation and comparison of SiRos1300 and SiRos1550 depth and resolution in 1% Intralipid relative to shorter wavelength SWIR-emitting dyes. (A) Schematic of 1% Intralipid depth experiment. All dyes were initially brightness-matched in CH_2Cl_2 on the SWIR camera and subsequently imaged at 0.5 mm depth increments using a 1,300, 1,400, or 1,500 nm LP filter. (B) Intensity plots at each 0.5 mm depth normalized to the brightest dye when using a 1,300, 1,400, or 1,500 nm LP filter. Note that the increased baseline in the 1,300 LP images is due to stray excitation light.

nature portfolio

Corresponding author(s): Jared H. Delcamp
Ellen M. Sletten

Last updated by author(s): Nov 26, 2023

Reporting Summary

Nature Portfolio wishes to improve the reproducibility of the work that we publish. This form provides structure for consistency and transparency in reporting. For further information on Nature Portfolio policies, see our Editorial Policies and the Editorial Policy Checklist.

Statistics

For all statistical analyses, confirm that the following items are present in the figure legend, table legend, main text, or Methods section.

n/a	Confirmed
☐	☒ The exact sample size (*n*) for each experimental group/condition, given as a discrete number and unit of measurement
☐	☒ A statement on whether measurements were taken from distinct samples or whether the same sample was measured repeatedly
☒	☐ The statistical test(s) used AND whether they are one- or two-sided *Only common tests should be described solely by name; describe more complex techniques in the Methods section.*
☒	☐ A description of all covariates tested
☒	☐ A description of any assumptions or corrections, such as tests of normality and adjustment for multiple comparisons
☐	☒ A full description of the statistical parameters including central tendency (e.g. means) or other basic estimates (e.g. regression coefficient) AND variation (e.g. standard deviation) or associated estimates of uncertainty (e.g. confidence intervals)
☒	☐ For null hypothesis testing, the test statistic (e.g. *F*, *t*, *r*) with confidence intervals, effect sizes, degrees of freedom and *P* value noted *Give P values as exact values whenever suitable.*
☒	☐ For Bayesian analysis, information on the choice of priors and Markov chain Monte Carlo settings
☒	☐ For hierarchical and complex designs, identification of the appropriate level for tests and full reporting of outcomes
☒	☐ Estimates of effect sizes (e.g. Cohen's *d*, Pearson's *r*), indicating how they were calculated

Our web collection on statistics for biologists contains articles on many of the points above.

Software and code

Policy information about availability of computer code

Data collection	Gaussian 16, Avagadro, Cary WinUV, Horiba FluorEssence, CHI602D Electrochemical Workstation, MATLAB
Data analysis	FIJI Distribution of ImageJ, Excel, Igor64

For manuscripts utilizing custom algorithms or software that are central to the research but not yet described in published literature, software must be made available to editors and reviewers. We strongly encourage code deposition in a community repository (e.g. GitHub). See the Nature Portfolio guidelines for submitting code & software for further information.

Data

Policy information about availability of data

All manuscripts must include a data availability statement. This statement should provide the following information, where applicable:

- Accession codes, unique identifiers, or web links for publicly available datasets
- A description of any restrictions on data availability
- For clinical datasets or third party data, please ensure that the statement adheres to our policy

The datasets generated during and/or analysed during the current study are available in a public repository https://zenodo.org/records/10079855 and are also available from the corresponding authors on reasonable request. Additional graphical data pertaining to: photophysical properties, electrochemistry, photoluminescent lifetimes, computation, micelle photostability, nanoemulsions, in vivo imaging, synthetic procedures, and NMR spectra are also available in the attached SI. Raw data for animal experiments can be accessed on BioImage archive #S-BIAD548.

Human research participants

Policy information about studies involving human research participants and Sex and Gender in Research.

Reporting on sex and gender	N/A
Population characteristics	N/A
Recruitment	N/A
Ethics oversight	N/A

Note that full information on the approval of the study protocol must also be provided in the manuscript.

Field-specific reporting

Please select the one below that is the best fit for your research. If you are not sure, read the appropriate sections before making your selection.

☒ Life sciences ☐ Behavioural & social sciences ☐ Ecological, evolutionary & environmental sciences

For a reference copy of the document with all sections, see nature.com/documents/nr-reporting-summary-flat.pdf

Life sciences study design

All studies must disclose on these points even when the disclosure is negative.

Sample size	The sample size for the chemical stability studies was 3 independent trials for each condition.
Data exclusions	No data was excluded from the chemical stability trials.
Replication	Each chemical stability study was conducted three separate times and all attempts showed similar results, indicating successful replication.
Randomization	Randomization was not necessary for the chemical stability studies.
Blinding	Blinding was not applicable for the chemical stability studies.

Reporting for specific materials, systems and methods

We require information from authors about some types of materials, experimental systems and methods used in many studies. Here, indicate whether each material, system or method listed is relevant to your study. If you are not sure if a list item applies to your research, read the appropriate section before selecting a response.

Materials & experimental systems

n/a	Involved in the study
☒	☐ Antibodies
☒	☐ Eukaryotic cell lines
☒	☐ Palaeontology and archaeology
☐	☒ Animals and other organisms
☒	☐ Clinical data
☒	☐ Dual use research of concern

Methods

n/a	Involved in the study
☒	☐ ChIP-seq
☒	☐ Flow cytometry
☒	☐ MRI-based neuroimaging

Animals and other research organisms

Policy information about studies involving animals; ARRIVE guidelines recommended for reporting animal research, and Sex and Gender in Research

Laboratory animals	Non-invasive whole mouse imaging was performed on athymic nude female mice (5-7 weeks old), purchased from Charles River Laboratories. The mice were housed in a 12-hour light/ 12-hour dark cycle. Room temperature was set at 73F (70-76), with humidity between 30-70%

Wild animals	No wild animals were used in this study.
Reporting on sex	All mice (4 total) in this study were female. Female was arbitrarily chosen as no significant differences with respect to light penetration of tissue was expected between the two sexes. Data with respect to males have not been collected.
Field-collected samples	No field samples were collected for this study.
Ethics oversight	Animal experiments were conducted in conformity with UCLA IACUC institutional guidelines (protocol number ARC-2018-047)

Note that full information on the approval of the study protocol must also be provided in the manuscript.